PNAS RESEARCH ARTICLE | EARTH, ATMOSPHERIC, AND PLANETARY SCIENCES

Upper mantle temperatures illuminate the Iceland hotspot track and understanding of ice–Earth interactions in Greenland

Parviz Ajourlou[a,1], Glenn A. Milne[a], Ryan Love[a], Juan C. Afonso[b,c], Farshad Salajegheh[c], Konstantin Latychev[d], Kristian K. Kjeldsen[e], Alexis Lepipas[a], Yasmina M. Martos[f,g], and Sarah A. Woodroffe[h]

Affiliations are included on p. 9.

Edited by David Kohlstedt, University of Minnesota Twin Cities, Minneapolis, MN; received March 2, 2025; accepted October 6, 2025

The thermal structure of the Earth beneath Greenland reflects the tectonic history of the region and impacts ice sheet evolution due to surface heat flow and the influence of temperature on Earth rheology, and thus glacial isostatic adjustment. We present results from a probabilistic joint inversion of multiple satellite and land-based datasets to determine the thermal structure of the lithosphere and upper mantle beneath Greenland and consider the implications for our understanding of the tectonic history, isostatic deformation, and Greenland ice sheet evolution. Passage of Greenland over the Iceland hotspot is well known but there remains considerable debate on the trajectory of this path. Our findings reveal strong lateral variability in thermal structure that is consistent with reconstructions of a west-to-east hotspot track across central Greenland. Applying our temperature model to infer mechanical properties of the solid Earth reveals viscosity variations reaching 3 orders of magnitude in the upper mantle. We generate an ensemble of plausible 3D viscosity models and produce quality fits to both paleo sea level and contemporary vertical land motion datasets. This result supports the veracity of our temperature model and questions the need for a large component of transient deformation to explain the observations. Our regional temperature and viscosity models can be used to develop improved reconstructions and understanding of past Greenland ice sheet changes and explore the influence of 3D Earth structure on simulating ice sheet and sea level evolution in the past and future.

glacial isostatic adjustment | Bayesian joint inversion | Greenland | hotspot

Significance

The Greenland continent is of interest due to its interaction with the Iceland hotspot and because it supports an ice sheet which is, and will be, a primary contributor to global sea level rise. Using multiple data sets, we estimate 3D temperature variations beneath Greenland and show that they are surprisingly large. Using these temperature variations, we are able to better constrain the path of the Iceland hotspot, and demonstrate their importance for explaining how the Earth deforms in response to ice sheet changes. Thus, our temperature model paves the way for better understanding the geological history of Greenland and the influence of ice–Earth interactions on ice sheet and sea level evolution.

Greenland has experienced an eventful tectonic history for the past ~90 Ma (1) with the opening of the Atlantic Ocean and the passage of the island over a mantle plume now located beneath Iceland (e.g., refs. 2 and 3). It is also one of only two land masses upon which ice sheets continue to exist on Earth during interglacial periods. These two aspects are interconnected, as recent tectonic events influence surface heat flux and the mechanical (rheological) properties of Greenland's crust and shallow mantle, both of which impact ice sheet evolution (4–7). This study considers both of these aspects by presenting an improved data-driven model of the thermal structure of the lithosphere and upper mantle in this region and exploring the implications of this knowledge for our understanding of both the regional tectonic history and late Quaternary ice sheet and sea level evolution.

The tectonic history of Greenland is reflected in the regional geology and geophysical properties of crustal and mantle rocks. Seismic imaging has revealed velocity heterogeneity that has been linked to the Iceland hotspot track (8–12). Determinations of geothermal heat flux (13, 14), lithosphere elastic thickness (15), and thermal structure (16) have also been used to infer the hotspot track. However, differences between these estimates, along with challenges in interpreting the results (10, 17) have hindered progress in this task. There is a clear need for improved data control and/or new approaches to make better use of the available observational constraints. One such approach is the use of multiple datasets with complementary sensitivities to rock properties such that a more robust inference can be made (8). Here, we present a multiobservable probabilistic inversion for the thermal structure of the lithosphere and upper mantle, focusing on the Greenland region. Our results, which include uncertainty estimates, indicate large spatial variations in temperature that can be used to improve constraints on the Iceland hotspot track and thus the tectonic/geodynamic history of this region.

The solid Earth influences the Greenland ice sheet (GrIS) by supplying heat to its base and vertical motion of the bedrock associated with isostatic adjustment, both of which impact several processes affecting GrIS evolution on multicentury

Author contributions: G.A.M. and J.C.A. designed research; P.A., G.A.M., and R.L. performed research; P.A., F.S., and K.L. contributed new reagents/analytic tools; P.A., K.K.K., A.L., Y.M.M., and S.A.W analyzed data; K.K.K., A.L., Y.M.M., and S.A.W provided input data; and P.A. and G.A.M. wrote the paper.

The authors declare no competing interest.

This article is a PNAS Direct Submission.

[1]To whom correspondence may be addressed. Email: pajou021@uottawa.ca.

This article contains supporting information online at https://www.pnas.org/lookup/suppl/doi:10.1073/pnas.2504752122/-/DCSupplemental.

Published December 8, 2025.

to millennial time scales (e.g., refs. 4, 7, and 18). The rate and amplitude of the isostatic adjustment are determined by the rheological properties of the underlying crust and mantle, which in turn are strongly controlled by temperature (e.g., ref. 19). Quantifying the isostatic response is necessary to simulate ice sheet evolution and constrain past changes in the GrIS using geological observations of relative sea level (RSL) change (20–22) and geodetic observations of vertical land motion (VLM, 23–25). A common assumption in most previous studies has been that the Greenland region is dominated by low temperatures and therefore a thick lithosphere and high viscosity mantle, typical of cratonic regions. Recent work (8, 24, 26) indicates that there is strong lateral variability in lithosphere thickness and viscosity that must be considered (27, 28) to accurately determine GrIS evolution in the past and future.

The work presented in the following sections includes three primary components: the development of a regional temperature model via joint inversion, the application of this model to infer 3D viscosity structure, and the use of these viscosity models to simulate RSL and VLM associated with GIA (*SI Appendix*, Fig. S1). In the next section, we describe the development of our temperature model, compare it to past inferences of thermal structure in the Greenland region, and consider the implications of our model for constraining the Iceland hotspot track. In the third and final section, we outline the procedures used to develop 3D viscosity models from our temperature inference and determine optimal viscosity parameters based on data-model fits to a regional paleo RSL dataset. Model fits to both RSL and VLM data are discussed in light of recent work highlighting the difficulty to fit both datasets (26) and the possibility of a large transient component in the isostatic response as a potential solution (27, 29).

Inference of 3D Temperature Model and Implications for the Iceland Hotspot Track

We consider multiple datasets within a probabilistic inversion framework that generates probability distributions of all model parameters (30–32, *Materials and Methods*). The general approach involves discretizing the study region into nonoverlapping columns, with the center of each column separated by 1° in latitude and longitude (*SI Appendix*, Fig. S2*A*). The inverted data were chosen due to their complementary sensitivities to thermal structure and included Rayleigh wave phase velocity dispersion curves, geoid anomalies, absolute elevation, and surface heat flow (*Materials and Methods*). Inversion results for temperature within one column are shown in *SI Appendix*, Fig. S2*B*.

The temperature-depth inversion results for each column were combined to generate a regional 3D temperature model (Fig. 1*A*). In continental Greenland, the most prominent temperature features include two regions of relatively cold material—in northwest and central eastern Greenland—that extend from beneath the crust to depths of ∼300 km (*SI Appendix*, Fig. S3). The more southerly feature is part of the well-known North Atlantic Craton, which hosts some of the oldest crustal rocks on Earth. Other prominent features are two regions of relatively hot material located in southern and central-eastern Greenland. We note that the amplitudes of these four features are well above the model uncertainty (Fig. 1*B*) and so they are robust aspects of the inversion. Since the lithosphere–asthenosphere boundary (LAB) represents a thermally controlled, rheological transition, we define the depth of this boundary using the 1,250 °C isotherm (33, Fig. 1*C*). As expected, the largest thermal anomalies are strongly reflected in our LAB depth model, with the thickest lithosphere located in northwestern and central-southern Greenland and the thinnest lithosphere found in southern and central-eastern Greenland. As is the case for temperature, these variations in LAB depth are well resolved by the constraining data (Fig. 1*D*).

Our thermal model shows greater spatial fidelity compared to that determined from a global shear wave velocity model (27), which reflects the increased spatial resolution of the regional surface wave dispersion curve data input to our analysis (34, *Materials and Methods*). While the spatial pattern is broadly similar (compare *SI Appendix*, Fig. S4 (200 km depth slice) to figure 4A in ref. 27), the greater spatial fidelity in our model better captures the amplitude of the temperature variations in the region. It is also notable that, while the regions of low temperature are of similar values at this depth (∼1,150 to 1,200 °C), the hotter regions (central-eastern Greenland) exhibit temperatures ∼100 °C greater in our model. A regional ambient noise tomography analysis (8) also shows a distinct hot region in central eastern Greenland. However, compared to our results, this analysis indicates a more prominent cold anomaly that extends from central to southern Greenland. Finally, the high-temperature region in southern Greenland is not inferred in either of these previously published models.

Several recent studies have estimated LAB depth in Greenland using different methods (e.g., refs. 10, 16, and 35). Of these three earlier studies, the results of ref. 35 (*SI Appendix*, Fig. S5*B*) compare most closely to our model, particularly in terms of the resolution and amplitude of LAB-depth variations. Over continental Greenland, the amplitude range is ∼200 km, although we note that the relative ranges are different [∼100 to 300 km in our model compared to ∼50 to 250 km (35)]. Since ref. 35 adopted 1,315 °C to define LAB-depth, their inferred temperatures are, in general, higher than those estimated here. Furthermore, the inferred LAB-depth values in northwest Greenland are different by as much as ∼150 km. The model of ref. 10 shows lower spatial resolution due to the limitations of the merged global velocity models, resulting in relatively uniform LAB depths across continental Greenland (*SI Appendix*, Fig. S5*C*). We do note, however, that some of the variations shown in this model (10): thicker values in the northwest and thinner values in central eastern and southern Greenland, correlate with our model and that of ref. 35. Other than the identification of thick lithosphere in central-western Greenland, the model of ref. 16 does not compare well with our results (*SI Appendix*, Fig. S5*D*). As a final comparison, we also consider results from an analysis that constrained lithosphere elastic thickness [(15), see their figure 2a]. While elastic thickness estimates cannot be compared directly with LAB depth, the spatial variations should show some correlation. This is generally the case, with this model indicating thick lithosphere in northwestern Greenland and relatively thin values in central eastern Greenland and in the far south.

Passage of the Iceland hotspot track has traditionally been inferred via reconstructing plate motion (e.g., refs. 2 and 3) with various other types of constraints also considered (e.g., refs. 6, 10, and 36). The inferred hotspot tracks show a large geographic spread, particularly for the older segment of the path (Fig. 2). This reflects the increasing uncertainty with age when reconstructing plate motion (e.g., ref. 37), as well as the lack of knowledge on the geology beneath the ice sheet and the broad geographic distribution of volcanic activity that is difficult to associate with a hotspot track (36). A recent study (17) concluded that, for the case of Greenland, where the passage of the plume was relatively recent (50 to 90 Ma) and much of the (preplume) continent was characterized by thick cratonic lithosphere, thermal erosion should be a primary indicator of the plume track. Based on this approach, our LAB-depth model suggests that tracks passing

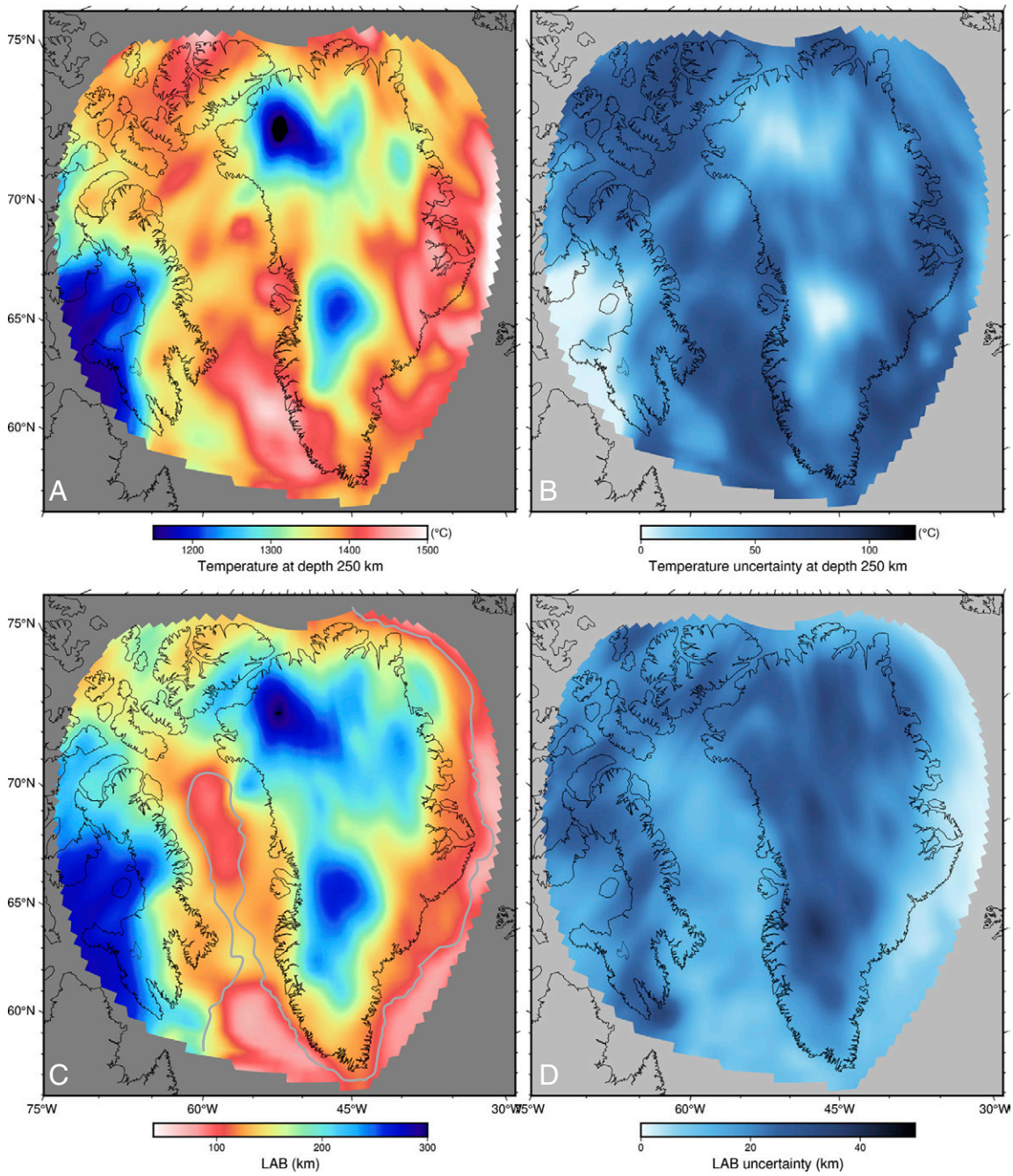

Fig. 1. Inferred thermal structure. Temperature (*A*) and the corresponding uncertainty (*B*) at 250 km depth. LAB depth (*C*) and the corresponding uncertainty (*D*). The gray contour in (*C*) indicates the approximate location of the continental shelf edge.

through northwest Greenland are unlikely. Our model favors paths with a west-to-east orientation that correlate well with areas of shallow LAB-depth (e.g., refs. 3 and 40). This interpretation is in agreement with recent seismic and geodynamic constraints (9, 10) and the location of flood basalts and the North Atlantic igneous Province in central east and west Greenland (42).

Inference of 3D Viscosity Model and Implications for Interpreting Sea-Level and Land Motion Observations

The 3D temperature models resulting from our joint inversion were used to determine a subensemble of 3D viscosity models for GIA simulations of deglacial RSL and present-day VLM. Given the high computational expense of the 3D Earth GIA model (e.g., ref. 43), we chose to limit the subensemble to 50 viscosity models. To ensure an accurate representation of uncertainty in the subensemble, we chose 25 temperature models that accurately reflect the ensemble mean and encompass a high-variance subset. These 25 temperature models were used to define lateral variability in viscosity relative to an average, depth-varying profile via an exponential dependence of viscosity on temperature (*Materials and Methods*). Uncertainty in the parameter that defines the strength of this dependence (ϵ, *Materials and Methods*) was accounted for by considering plausible end-member values for this value, giving a total of 50 laterally variable viscosity models that we use to estimate uncertainty in our simulations of RSL and VLM. Using the average of the 25 temperature

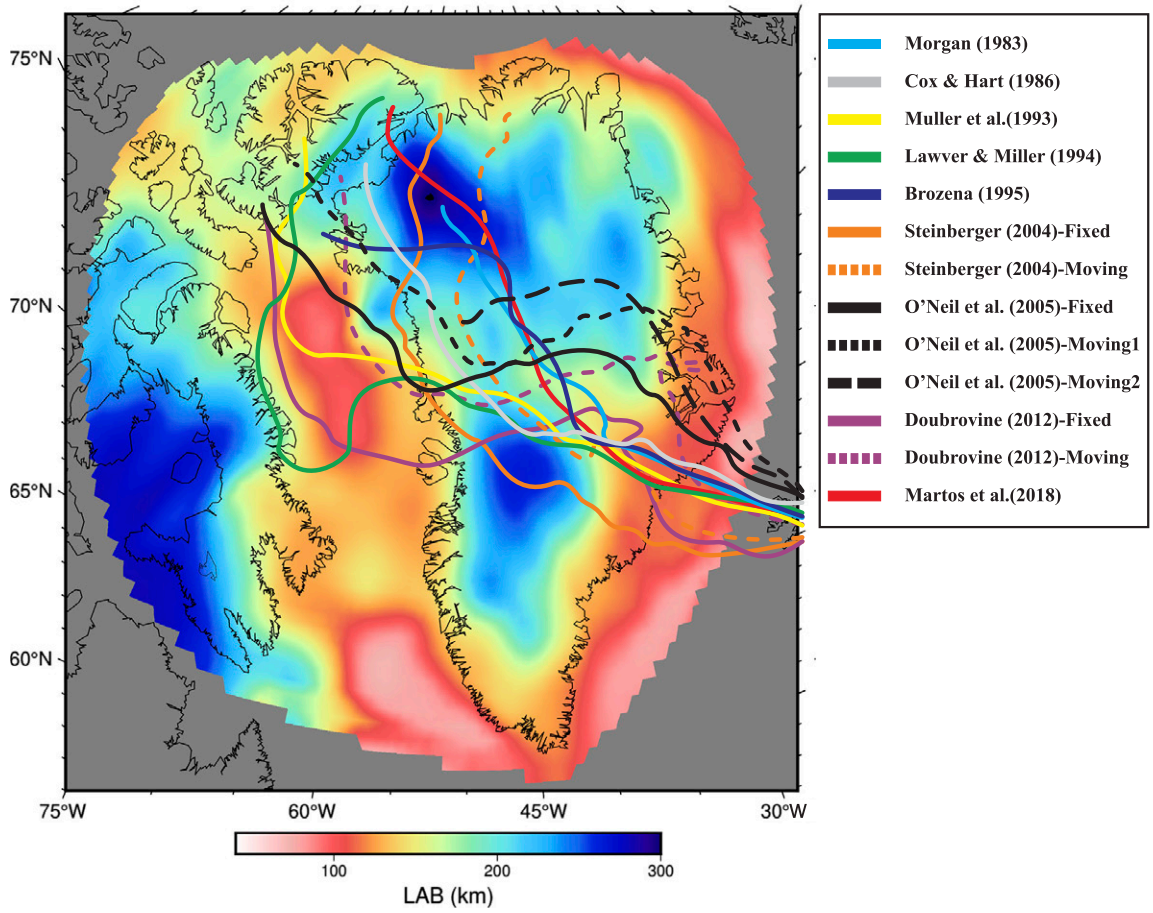

Fig. 2. LAB depth overlain by reconstructed Iceland hotspot tracks from previous studies (2, 3, 14, 37–41, see key). The key also indicates whether a fixed (solid line) or moving (dashed line) hotspot was assumed.

models, we show lateral viscosity variations at six depth slices in *SI Appendix*, Fig. S6. These results indicate that viscosity variations reach three orders of magnitude in the shallow upper mantle beneath Greenland. The 50 regional viscosity models, spanning the region defined in *SI Appendix*, Fig. S2 and extending to a depth of ~400 km, were embedded within a global viscosity model (*Materials and Methods*; *SI Appendix*, Fig. S7). A global Earth model is required to produce accurate computations of sea-level changes and land motion for a specified ice loading history and Earth viscosity model (*Materials and Methods*).

To quantify the impact of lateral variability in Earth viscosity structure on RSL and VLM, we define a radial (1D) viscosity model on which to superimpose the 50 realizations of lateral structure described above, and compare output from these 3D Earth model simulations to the output from the 1D Earth model. Using a deglacial ice sheet reconstruction of GrIS evolution (22), we determined optimal values for a three-parameter radial model (specifically, lithosphere thickness (LT), and viscosity in the upper and lower mantle regions—abbreviated to UMV and LMV, respectively) using both the 3D and 1D Earth models. These parameter values were optimized based on minimizing data-model misfit to a quality-assessed regional RSL dataset (*Materials and Methods*; *SI Appendix*, Fig. S8). A total of 484 combinations of the LT-UMV-LMV radial model parameters were considered in this process. Given the high computational expense of the 3D Earth model, exploring such a large parameter space required the use of an emulator (44) (*Materials and Methods*). For the 1D case, optimal radial parameters are a 120 km lithosphere, an UMV of 5×10^{20} Pas, and a LMV of 10^{21} Pas. This inference is compatible with that of ref. 22 who considered a similar RSL dataset and the same radial parameterization of viscosity structure. For the 3D case, the optimal parameters are, respectively, 71 km and 10^{21} Pas in both upper and lower mantle regions. Thus, a significant bias is produced when inferring radial structure without accounting for lateral variability (e.g., refs. 45 and 46).

The modeled RSL signal at 8 kyr B.P. shows the typical pattern of high sea levels in areas characterized by ice retreat (*SI Appendix*, Fig. S9) and negative values adjacent to these regions (Fig. 3 *A* and *B*). While the spatial pattern for the 1D and 3D cases is broadly similar, reflecting the use of the same ice loading model, there are important differences in the geometry and amplitude of this pattern that reflect the additional viscosity structure in the 3D Earth model. For example, RSL is considerably lower in northwest Greenland in the 3D case which is consistent with thicker lithosphere and lower viscosity in this region resulting in an isostatic response of diminished amplitude. RSL is also lower in central eastern Greenland. However, in contrast to the results for northwest Greenland, the lower RSL values are explained by the presence of lower viscosity values causing a more rapid isostatic adjustment (uplift) following ice retreat (Fig. 3*D*). Differences in RSL at 8 kyr BP between the 3D and 1D Earth model simulations exceed 10 m in many coastal areas. There is also considerable uncertainty in the signal associated with lateral Earth structure, with values also exceeding 10 m in some areas at 8 kyr BP (Fig. 3*C*). Data-model comparisons for all RSL sites considered are provided in *SI Appendix*, Fig. S10. These results

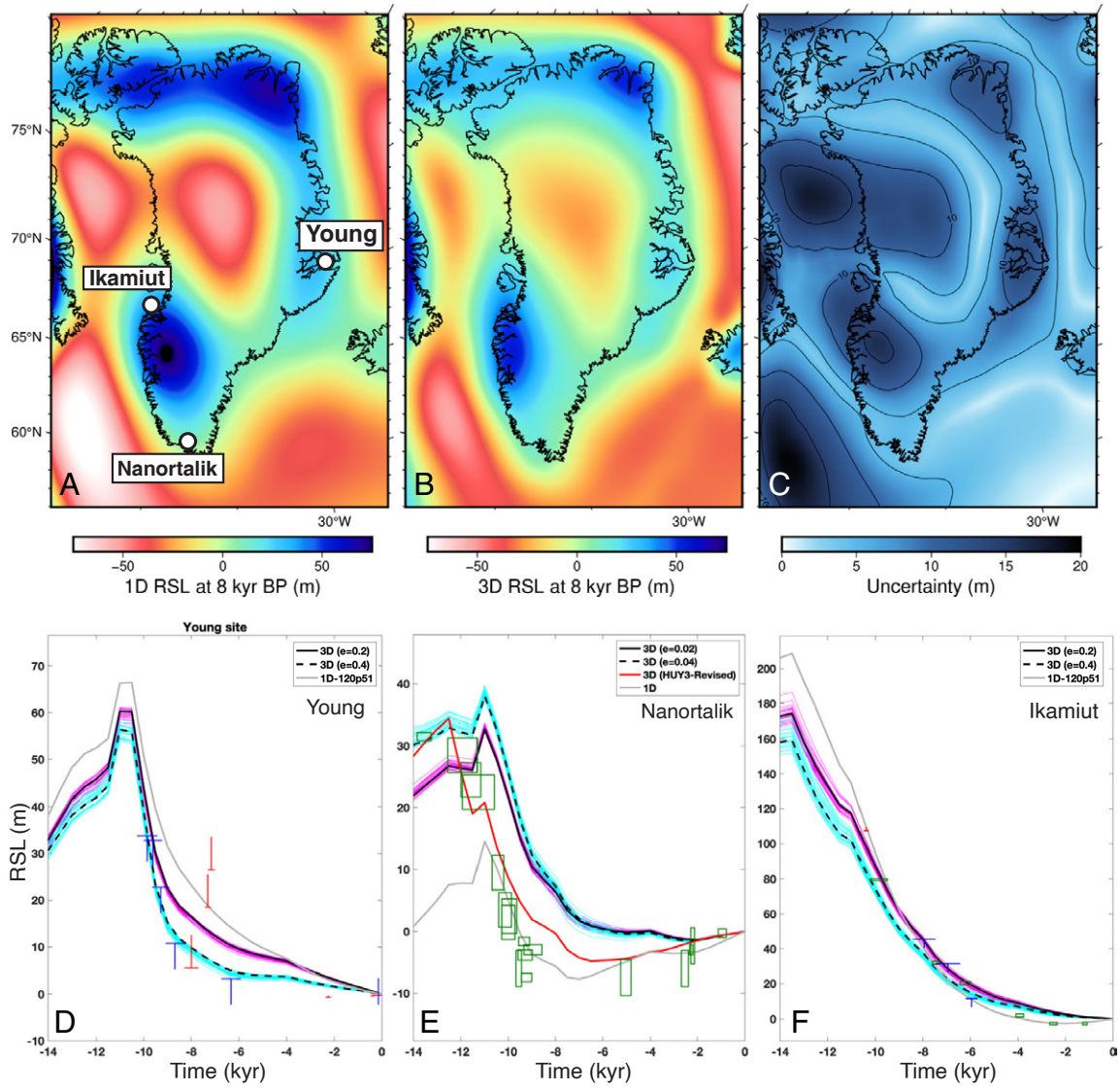

Fig. 3. Modeled RSL changes at 8 kyr BP for (*A*) the optimum 1D reference model (LT = 120 km, LMV = 5×10^{21}, and LMV = 1×10^{22}), and (*B*) the optimum 3D Earth model calculated using the 1D reference model (LT = 71 km, UMV and LMV = 1×10^{22}) and the mean of the 50-model subensemble (*Materials and Methods*). (*C*) RSL range at 8 kyr BP based on the 50-model subensemble. *Lower* plots show RSL data-model comparisons for the 1D and 3D Earth models at three sites: Young (*D*), Nanortalik (*E*), and Ikamiut (*F*) (locations shown in *A*). Green boxes and blue and red markers are SLIPs, marine limiting points, and terrestrial limiting points, respectively. RSL for the optimum 1D viscosity model is shown by the gray lines. RSL for the 50 3D models is shown by cyan and magenta lines, for $\epsilon = 0.02$ and $0.04\ ^{\circ}C^{-1}$, respectively (solid and dashed black lines are the average of these subensembles). The red line for the Nanortalik site shows the RSL prediction based on the revised ice model (see main text) and a 3D viscosity model determined using $\epsilon = 0.03\ ^{\circ}C^{-1}$ and the mean of the temperature inversions (Fig. 2 and *SI Appendix*, Fig. S4).

indicate that the signal associated with lateral Earth structure, and its uncertainty, generally increase with age at most locations.

We highlight RSL results at three sites (Young, Nanortalik and Ikamiut; Fig. 3 *D–F*; locations in-frame *A*) as they illustrate the impact of lateral viscosity variations in three key regions. The site Young is located in eastern Greenland where mantle temperatures are relatively high. As a result, the isostatic response is more rapid, resulting in a modeled RSL curve that drops more sharply compared to the optimal 1D case. Such a rapid RSL fall is necessary to capture the limiting data at this location. At Nanortalik (Fig. 3*E*), past work has indicated difficulty in matching the RSL amplitude and rate of fall (22, 47, Fig. 3*E*, solid grey lines), which has led to the suggestion of glacially triggered faulting (48) to capture the older data points (above ∼20 m). Our temperature model indicates relatively thin lithosphere and low viscosity in this region which results in a larger amplitude RSL response compared to the 1D model (Fig. 3*E*). However, this also leads to a poorer fit due to the modeled curve sitting too high for most of the Holocene. Based on data constraints on the timing of major ice retreat in this region (49), it occurs too late by 1 kyr or more in the ice model used here. By revising this aspect of the ice model, an improved fit can be obtained (solid red curve in Fig. 3*E*). Further improvements to the fit can likely be achieved by making additional changes to the ice model but this is beyond the scope of the present analysis. Finally, the Ikamiut site is close to a region of relatively thick lithosphere and high viscosity, resulting in RSL curves of diminished amplitude and reduced rate of RSL fall. In this area, the 3D Earth models perform well in the mid-Holocene but they do not capture the negative RSL lowstand that, although of small amplitude, is a robust feature of the observations at several sites in this region (*SI Appendix*, Fig. S10) and reflects the relative amplitude of signals

due to local and nonlocal ice (50, see their figure 18). The results for these three sites illustrate the significant impact of lateral Earth structure on fitting and interpreting RSL observations in Greenland and indicate how our 3D viscosity model provides a path toward developing improved models of GrIS deglaciation.

A summary of the data-model misfit values (*Materials and Methods*) for different subregions as well as for all of Greenland is provided in *SI Appendix*, Table S3. [Note that RSL data from northwest Greenland were excluded from this analysis due to documented inaccuracy of the ice model in this region (51).] While the Greenland-wide quality of data-model fit is improved for the 3D case relative to the 1D case, the improvement is modest and there is regional variability in which class of Earth model provides the best results (*SI Appendix*, Table S3). For example, the 3D Earth model produces significantly better fits in northeast Greenland (blue circles in *SI Appendix*, Fig. S8)—though we note that the data are generally of poor quality in this region (consisting mainly of limiting constraints). The 1D Earth model produces better fits in central-east Greenland (green circles in *SI Appendix*, Fig. S8). By far the poorest fits, for both classes of model, are in southern Greenland. The ice model used here was tuned primarily to match ice extent (margin) constraints; however, where these data are sparse, ice model parameters were chosen to better match RSL constraints (22). Since a 1D Earth model was applied in this tuning exercise, the resulting ice model will be biased due to the neglect of lateral variations (Fig. 3). The influence of lateral Earth structure primarily impacts the amplitude of the RSL response rather than the timing of initial RSL fall (*SI Appendix*, Fig. S10), so this bias will be more pronounced in the inferred ice thickness distribution rather than the chronology.

Results for present-day VLM rates also indicate a large signal associated with lateral viscosity structure (compare frames *B* and *C* in Fig. 4), with amplitude differences exceeding 1 mm/yr in many areas. The ice history model used to calculate VLM rates is different to that used to generate the RSL results (Fig. 3). Recent work has demonstrated the importance of ice sheet changes since the Little Ice Age (LIA) maximum (~1,900) to accurately model present-day rates of VLM in Greenland where regions of relatively low viscosity are postulated to exist—either via a significant transient component in the isostatic response (29), a low viscosity asthenosphere layer (52), or due to passage of the Iceland hotspot (28). Therefore, in addition to changes included in the deglacial model (up to 1 kyr BP), we included LIA changes associated with the ice sheet (53) and changes in peripheral glaciers (54) (*Materials and Methods*). The relative contributions of these different ice loading components to the modeled VLM are strongly controlled by the adopted Earth viscosity model (*SI Appendix*, Fig. S11). The low viscosity region in central eastern Greenland that we associate with the hotspot track amplifies the signal due to ice sheet and glacier changes during the 20th century (compare *SI Appendix*, Fig. S11 *B* and *C* with, respectively, *E* and *F*). Specifically, these component VLM signals are amplified from being a few tenths of a mm/yr for the optimal 1D Earth model to order mm/yr—and up to ~6 mm/yr in central eastern Greenland—for the optimal 3D viscosity model. These high rates for central eastern Greenland associated with recent ice loading are consistent with those of ref. 28.

There is considerable uncertainty in our knowledge of ice sheet changes leading into and following the LIA maximum (55). For this reason, we considered a range of plausible chronologies for the ice sheet changes and a conservative ±20% range in the total amplitude of thickness change from the LIA maximum to present in this component of the ice model (*Materials and Methods*). The same amplitude scaling was used to estimate uncertainty in the peripheral glacier changes. Modeled VLM rates, including deglacial and recent loading changes for 3D and 1D Earth models, are provided in Fig. 4*D*. The addition of lateral viscosity structure results in much improved fits to the GNSS data compared to those for the (RSL-optimized) 1D Earth model. The quality of fit for the 3D Earth model is remarkable, given that no model parameters were tuned to match the VLM rates. While there remain some stations where the model does not capture the observed VLM rates, these can likely be explained by uncertainties and limitations in the ice models considered here. One notable simplification is that ice extent changes were assumed to be spatially synchronous during and following the LIA. Observations from aerial imagery and historical observations show considerable Greenland-wide variability of the post-LIA maximum retreat, even for nearby outlet glaciers. Thus, a scenario of spatial synchroneity in ice advance into and retreat from the LIA is overly simplistic (55). An important outcome of this study is the demonstration that improved decadal- to century-scale ice chronology models are required to accurately interpret the observed VLM rates in central and southern Greenland.

The ability of our GIA model to produce quality fits to both paleo RSL data and contemporary VLM rate observations has relevance for recent work that has identified and sought to explain why models tuned to fit one of these datasets provides poor fits to the other (26, 27, 29, 52). While our results do not exclude the importance of a significant transient signal in the GIA response (27, 29), they provide an alternative explanation to this problem and highlight the need for improved data control to separate these signals. Our results partially support those of ref. 52 in that our inversions indicate sublithosphere regions with low viscosity in central eastern Greenland. However, there is considerable lateral variability in this structure that is not accommodated with 1D (spherically symmetric) Earth models.

Our temperature model supports and extends past work to demonstrate that the Greenland region exhibits strong lateral variability in the lithosphere and shallow upper mantle. Our temperature model can be used in a variety of applications, such as the testing and development of geodynamic models (e.g., ref. 10). It can also be used alongside mineral physics constraints to further explore and test more sophisticated rheological models of the isostatic response (e.g., ref. 27). Better constraints on this response are necessary for developing improved reconstructions and understanding of past GrIS changes (22, 24, 56) and producing more accurate simulations of future GrIS evolution (7, 57) to quantify the impact on ocean circulation (58) and global sea levels (59).

Materials and Methods

Joint Inversion for Thermal Structure.

Inversion method. We adopt a multiobservable probabilistic inversion approach (30–33) utilizing a Bayesian framework to jointly invert multiple geophysical datasets (33). This approach has been developed and coded into a Fortran package: LitMod1D_4INV to provide estimates of the thermal and primary elemental composition of the lithosphere and underlying upper mantle. The general solution to the inverse problem over the parameters of interest ($\mathbf{m}$) is represented by a multidimensional probability density function (PDF), known as the posterior PDF. For parameter estimation problems, this PDF can be written as (30, 60) $\sigma(\mathbf{m}) \propto \rho(\mathbf{m})L(\mathbf{m})$, where $\rho(\mathbf{m})$ is the prior over $\mathbf{m}$ (describing information about $\mathbf{m}$ independently from the data, $\mathbf{d}$) and $L(\mathbf{m})$ is the likelihood function, which encodes the data-model misfit properties (60). More details on the likelihood function can be found in previous studies (e.g., refs. 33, 61, and 62).

The numerical value ascribed to the weights in the likelihood function depends on the type of dataset being considered. Previous work has shown

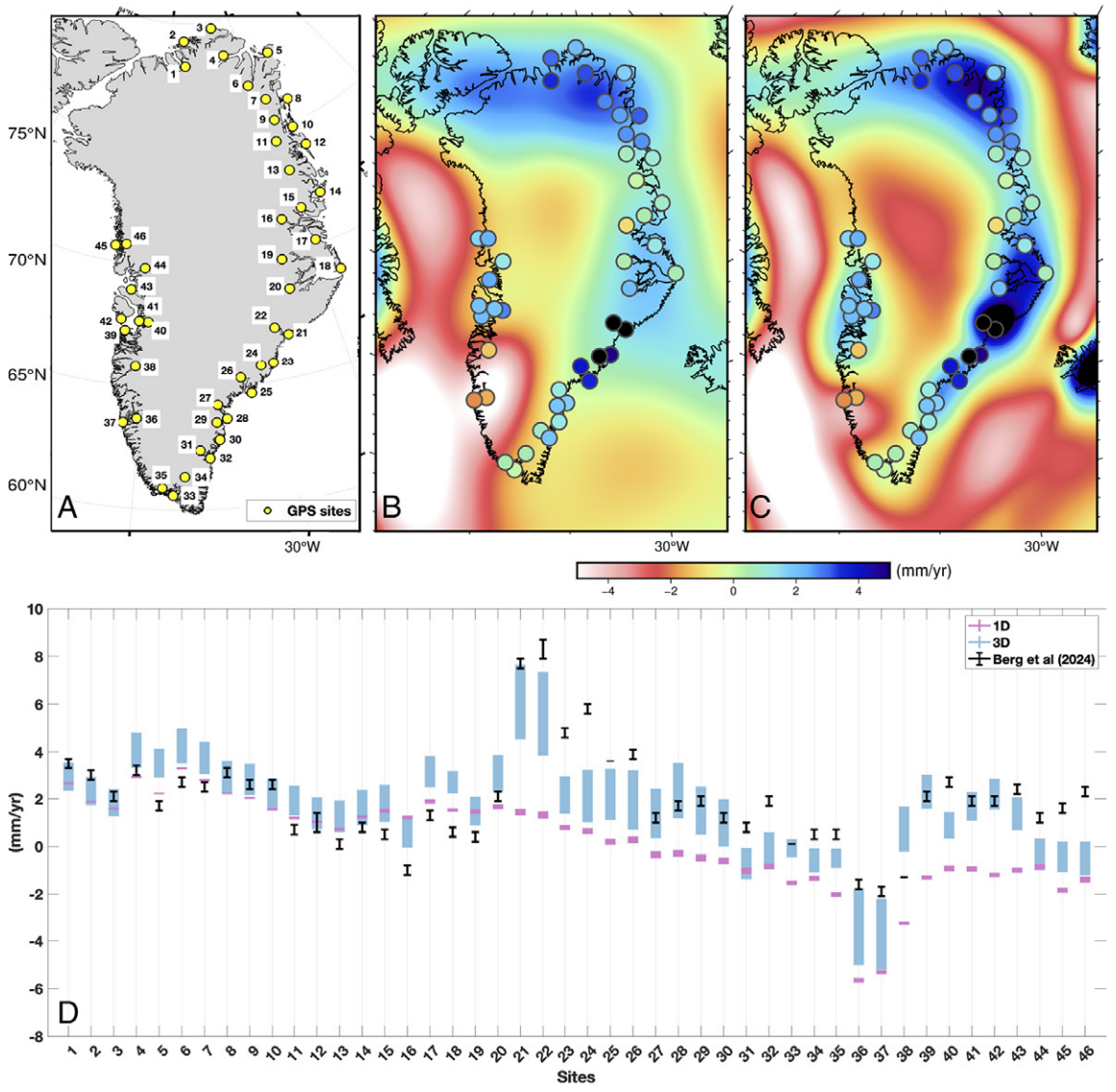

Fig. 4. (*A*) The location of the GNSS stations considered in this study. We do not include stations in northwest Greenland due to inaccuracy in the adopted deglacial ice model for this region (22, 51). Modeled VLM rates using the optimal 1D Earth model (*B*) and the optimal 3D Earth model (*C*) that include deglacial and more recent loading signals associated with the ice sheet and peripheral glaciers (see text). (*D*) Modeled and observed VLM at the stations shown in (*A*). The pink and blue bars show the range of values obtained when considering uncertainty in the LIA and peripheral glacier loading for the optimal 1D and 3D Earth models. The pink bars also consider the range determined from the deglacial ensemble of 50 3D Earth model simulations (see text).

that seismic constraints provide better sensitivity to the first-order thermal structure compared to the other input datasets, which are generally needed to increase the sensitivity to the compositional structure (30, 33). Therefore, a weighting scheme was chosen to obtain models that fit seismic constraints as well as possible while being simultaneously consistent with, but not dominated by, nonseismic data (61). The choice of seismic constraints will largely govern the output of the temperature inversion (63) and so it is important to choose the constraints that are best suited to the problem at hand. The recent Rayleigh wave tomography model (34) was specifically developed to constrain upper mantle structure in the circum-Greenland region to depths of 300 to 400 km. In fact, this study was performed to feed into a LitMod inversion for the purpose of improving GIA models for Greenland (61). Further details on these input seismic constraints are provided in *Data* subsection below.

The posterior PDF for our problem has no closed-form solution, so we sample it using the Delayed Rejection Adaptive Metropolis (DRAM) of ref. 64. Based on results from previous studies (33, 65), we run 300,000 simulations for each grid point to estimate the Earth properties with depth, amounting to a total of ~150,000,000 simulations for our region.

Model parameterization. The 3D volume of Greenland and northeastern Canada consists of 446 nonoverlapping columns in a 1° × 1° grid (*SI Appendix*, Fig. S2*A*). Each 1D column is defined by three crustal layers (i.e., sediment/ice, upper, and lower crust) and two mantle layers (lithospheric and sublithospheric mantle). For glaciers in the Canadian Arctic, only major glaciers with large spatial extent are considered, and in areas with no ice, the first layer is defined as a sediment layer. Each crustal layer is characterized by seven parameters: thickness perturbation (Δh), coefficient of thermal expansion (α), bulk density at surface pressure–temperature (P-T) conditions [$\rho(P_0, T_0)$], thermal conductivity (κ), compressibility (β; also given by the ratio of seismic velocities V_P/V_S), and radioactive heat production (RHP). Since the inversion results are heavily affected by variations in RHP, ρ, Δh, and V_P/V_S (33), these parameters are considered unknown to within a defined prior range (*SI Appendix*, Table S1) and solved for in the inversion. The remaining parameters (α, κ, β) are treated as constants (*SI Appendix*, Table S2).

Similar to previous studies (30, 33, 66, 67), we discretize the 1D column (crust and upper-mantle) with a 2 km finite-difference mesh (*SI Appendix*, Fig. S12*B*) to calculate elevation, lithospheric geotherms, and geoid height. Also, the upper mantle is discretized into 15 thermodynamic nodes (*SI Appendix*, Fig. S12*B*) to

calculate equilibrium mineral assemblages and corresponding thermo-physical properties (e.g., V_p, V_s, ρ) via a Gibbs free-energy minimization problem. The number of thermodynamic nodes within the two mantle domains depends on the lithospheric thickness. In ocean areas, where the lithosphere is thin, we use eight thermodynamic nodes in the lithosphere and seven in the sublithospheric mantle. In contrast, in continental areas, we use ten thermodynamic nodes in the lithosphere and five below the lithosphere.

Based on the strong correlation between temperature and rock strength (33) and numerical results of upper mantle convection with realistic viscosities (68–73), we consider the 1,250 °C isotherm ($T_{1,250}$) to correspond to the bottom of the lithosphere, defining the depth to the lithosphere–asthenosphere boundary (LAB). The sublithospheric isotherm is constructed via linear interpolation using the temperatures at three depths, T_{buffer}, T_{inter}, and T_{bottom}, retrieved by the inversion (*SI Appendix*, Fig. S12*B*). We refer the reader to refs. 30, 31, and 33 for details on this method.

The LitMod framework infers the thermochemical structure of the lithosphere under the assumption of a static system. As a result, dynamically evolving components such as topography and the geoid may introduce error in the inferred density structure in regions that are not in isostatic equilibrium, such as Greenland. In such cases, the dynamic component of topography is effectively accommodated during the inversion process through minor adjustments to the density structure distributed across a broad depth range. A similar mechanism applies to the geoid anomaly, though it exhibits heightened sensitivity to the depth distribution of density variations. These adjustments typically remain well within the posterior uncertainty bounds of the inferred model parameters and are therefore unlikely to introduce significant bias into the inversion results. Extensive numerical tests and sensitivity analyses conducted in prior studies (e.g., refs. 30, 33, and 74) demonstrate that the lithospheric architecture derived using LitMod is robust against dynamic topography or unrelaxed isostatic contributions of up to several hundred meters. This is approximately an order of magnitude greater than the isostatic land motion expected in the future associated with the most recent deglaciation of the GrIS.

Data. The seismic constraints include Rayleigh and Love wave phase velocity dispersion curves (PVDCs) for 30 periods ranging from 25 to 185 s (*SI Appendix*, Fig. S13). Rayleigh wave PVDCs were extracted from a recently published phase velocity model for Greenland and northeastern Canada (34) that provides the best available spatial resolution and extent for the aims of this study (61). Love wave PVDCs were calculated from the Rayleigh wave velocity model and the radial anisotropy extracted from a recent North Atlantic shear wave velocity model (75). Including both Rayleigh and Love wave information results in a more accurate determination of temperature (61). Since the uncertainty in dispersion curves increases with depth, we allocate an uncertainty that linearly increases from one percent at 30 s to two percent at 185 s. To mitigate the effect of deep (>400 km depth) and unmodeled velocity anomalies in long-period phase velocities, we extended the velocity model to a depth of 1,000 km by incorporating the global GypSum model (76).

Nonseismic datasets include elevation data (*SI Appendix*, Fig. S14*A*) from the international GEBCO bathymetry dataset, geoid height (*SI Appendix*, Fig. S14*B*) extracted from the Gravity field model, XGM2016 (77). The input means and associated SDs for elevation and geoid were calculated on a 1° × 1° grid from their original high-resolution datasets. Minimum values associated with modeling errors were added to the observed SDs for elevation (150 m) and geoid (0.8 m) data. For surface heat flow, a composite dataset (*SI Appendix*, Fig. S14*C*) was used. Data from ref. 14 was used over Greenland (including the continental shelves), and, for the rest of our study region, data from ref. 78 was used (spatial smoothing was applied to prevent any sharp and unrealistic changes at the boundaries between these datasets). The initial crustal model was obtained from CRUST1.0 (79), and the ice thickness information was obtained from IceBridge BedMachine (80) for Greenland and the results from ref. 81 were used for the Canadian Arctic.

Generating 3D Viscosity Models.

Regional models. There are two general aspects to this component of the analysis. First, the temperature models resulting from the LitMod inversion were used to determine relative viscosity structure via the relationship

$$\tilde{\eta}\,(r,\theta,\phi) = \exp\left(-\epsilon\,\delta T\,(r,\theta,\phi)\right), \quad [1]$$

where $\tilde{\eta}$ is the absolute viscosity relative to the reference (radial) viscosity (η/η_{ref}), δT is the difference in temperature relative to the mean value for a given depth within the study region, ϵ is a parameter that defines the amplitude of the viscosity variations for a given temperature field, and r, θ, and ϕ are the radius, colatitude, and east longitude. We compute variations in temperature and viscosity relative to the mean at a given depth as the radial viscosity structure is determined via a data model comparison (*GIA Modeling*).

To estimate uncertainty in our models of regional viscosity structure, we subsampled our temperature inferences to define a high variance set of 25 models that accurately capture the mean of the full ensemble at any given grid node (*SI Appendix*, Fig. S15). This subensemble was used, along with two end member ϵ values of 0.02 and 0.04 °C^{-1} to generate 50 realizations of lateral viscosity variations to represent uncertainty in this field. Viscosity values based on the mean of the 25 temperature-model subensemble and an ϵ value of 0.03 °C^{-1} is shown in *SI Appendix*, Fig. S6 for six different depths. To complete this suite of regional Earth viscosity models, lithospheric thickness was determined by equating this value to the depth of the 1,250 °C isotherm in each of the 25 models of the subensemble.

We acknowledge that other factors not considered here, such as grain size and water content, can also influence the viscosity of mantle material (19). Including additional data types in the inversion could provide useful constraints on the role of these other factors (e.g., ref. 82).

Global models. To accurately simulate RSL and VLM associated with GIA, it is necessary to solve the sea-level equation (*Glacial Isostatic Adjustment Modeling*) and so a global Earth model is required. We chose to combine two global seismic velocity models to generate a single global viscosity model, into which we could then insert our regional Greenland model. We combined the global model S40RTS (83) and the higher-resolution model SL2013sv (84) such that the latter defines shear wave velocity structure in the upper mantle and the former defines this structure in the lower mantle. To avoid numerical artifacts, the velocity perturbations were interpolated over a depth range of several hundred km in the shallow lower mantle. Following previous studies (e.g., refs. 26, 43, and 85), the conversion from shear wave velocity to temperature was performed via the relationships

$$\delta \ln \rho\,(r,\theta,\phi) = \frac{\partial \ln \rho}{\partial \ln V_S}\,(r)\,\delta \ln V_S\,(r,\theta,\phi),$$
$$\delta T\,(r,\theta,\phi) = -\frac{1}{\alpha(r)}\,\delta \ln \rho\,(r,\theta,\phi), \quad [2]$$

where V_S, ρ, and δT are the perturbations in shear wave velocity, density, and temperature, respectively and $\frac{\partial \ln \rho}{\partial \ln V_S}$ is a depth-dependent scaling factor.

For a global lithosphere model, we chose LithoRef18 (86) as it was constructed using a similar methodology to that used in our regional analysis. LAB depth in LithoRef18 is defined as the depth to the 1,300 °C isotherm. To make the global and regional LT models compatible, we created a revised version of LithoRef18 by using the 1,250 °C isotherm from the inferred temperature profiles to define LAB depth. *SI Appendix*, Fig. S7 illustrates our viscosity and lithosphere models and how well our regional models fit into the chosen global models.

Glacial Isostatic Adjustment Modeling.

GIA datasets. Holocene RSL data points used in this project are taken from ref. 22, but with some new data added. RSL height at a specific time is reconstructed in different locations, and data are grouped into 60 sites (*SI Appendix*, Fig. S8*A*). These sites are mostly concentrated in western and eastern Greenland with two distinctive spatial gaps in northwestern and southeastern Greenland. The temporal and height distribution of RSL points is illustrated in *SI Appendix*, Fig. S8*B*. In total, the dataset comprises 123 sea level index points, 741 marine limiting points, and 172 terrestrial limiting points and primarily spans the period ∼10 kyr BP to present). In the Early Holocene, RSL around Greenland varies by more than 100 m, demonstrating significant spatial variations in the amplitude of the isostatic response.

Contemporary rates of VLM are determined from Greenland's GNSS Network (GNET, e.g., ref. 24). These VLM data include signals associated with surface

loading on different timescales within Greenland and further afield (24, 25). We use the GIA-related VLM rates determined by ref. 25 but exclude stations in northwest Greenland given limitations of our adopted ice model in this region (51). These GIA-related VLM rates (Fig. 4 *B-D*) illustrate a nonuniform vertical velocity field across Greenland. Most rates are in the range 0 to 4 mm/yr except for the relatively high values in southeastern Greenland and low values in southwestern Greenland.

Forward models. For the 3D Earth simulations, we adopt the Seakon model of ref. 43. This model is based on a numerical finite-volume approach using a multilayered, spherical tetrahedral grid. Grid resolution (vertically and laterally) decreases with depth. For example, lateral resolution varies from ∼15 km near the surface to ∼50 km at the CMB. The 1D Earth simulations are based on the computation of viscoelastic Love numbers (87, 88). For both types of Earth models, sea-level changes (ocean loading) were computed by solving the extended sea level equation (89, 90) to ensure that coastline migration is accounted for. The influence of Earth rotation on GIA is also included (91, 92). For the 1D Earth model a spherical harmonic truncation of degree and order 256 was used.

Ice loading models. Three different ice loading models were used in this analysis. To capture ice thickness variations prior to and following the last glacial maximum, we adopted the ice model reconstruction of ref. 22. This ice model is the most recent reconstruction of deglacial GrIS changes based on fitting GIA-related (RSL) observations from Greenland. As noted above, this model is known to significantly underestimate ice thinning in northwest Greenland during the Holocene (51). Therefore, we exclude RSL and VLM data from this region in our analysis. In regions of relatively low viscosity, recent changes in ice extent can significantly contribute to present-day VLM rates (28, 29, 93). Extent changes on century timescales are not resolved in our adopted deglacial model and so we considered ice thickness changes of the GrIS associated with the build up to and retreat from the Little Ice Age (LIA, 53) and changes in glaciers peripheral to the ice sheet during the 20th century (54).

We considered a small suite of LIA ice loading histories based on the results of ref. 53 where the build up to the LIA maximum (defined to be 1880 in our model) was characterized by either: i) a steady growth over ∼900 y or ii) a rapid growth over ∼100 y and stable thickness for the remaining ∼800 y. Ice retreat (thinning) from the LIA maximum to 1981 was defined to be either linear, or nonlinear with a large mass loss in the first half of the 20th century, concurrent with a regional warming event (94). The ice sheet changes from 1983 to 2010 in ref. 53 are also included. In addition to these different time histories, a ±20% scaling in ice thickness was adopted to sample the large uncertainty in the ice thickness changes leading up to and following the LIA maximum (55). To define the spatial extent of peripheral glacier changes, we followed the methodology described in ref. 95. In short, we used the Randolph Glacier Inventory (release 5.0) to define the present-day ice extent and simply scaled the resulting ice thickness values to reproduce the mass change estimates provided by ref. 54 for the period 1902 to 2010. We compute the nonelastic contribution of these recent loading signals to VLM rates for the period 2010 to 2020 by ensuring no ice sheet or glacier changes post 2010.

Determining optimal 1D and 3D viscosity models. As noted above, the lateral viscosity structure models were superimposed on a radial viscosity profile that results in optimal fits to the adopted RSL database. This viscosity profile is defined via three parameters: lithosphere thickness, viscosity in the upper mantle (base of lithosphere to 670 km depth), and viscosity in the lower mantle (670 km to the Core–Mantle Boundary). This is a standard viscosity-depth parameterization for 1D (spherically symmetric) Earth models. In seeking optimal parameters based on model fits to the RSL dataset, the following parameter ranges were considered: lithosphere thickness (46 to 120 km), upper mantle viscosity (0.05 to 1 $\times$ 10^{21} Pas), lower mantle viscosity (1 to 90 $\times$ 10^{21} Pas); giving a total of 484 parameter sets.

The optimal parameter set was identified by minimizing a data-model misfit defined as $\delta_{\text{Total}} = \delta_{\text{SLIP}} + \delta_{\text{Lim}}$, where δ_{SLIP} and δ_{Lim} are the misfit contributions associated with sea level index points (SLIPs) and limiting data, respectively. The contribution from limiting data is normalized since limiting data provided only a one-sided constraint on past RSL. In the case of SLIPs, the data-model misfit is calculated based on the minimum distance (L2-norm or Euclidean distance) between each SLIP and the modeled RSL. The misfit for SLIP data is calculated via (96):

$$\delta_{SLIP} = \frac{1}{N}\sqrt{\sum_{n=1}^{N}\left(\left(\frac{\Delta}{\sigma}\right)^2_{RSL,n} + \left(\frac{\Delta}{\sigma}\right)^2_{t,n}\right)}\ , \qquad [3]$$

where $\Delta_{RSL,n}$ and $\Delta_{t,n}$ are the observed and modeled RSL difference for the nth observation in height and time, respectively. $\sigma_{RSL,n}$ and $\sigma_{t,n}$ are the RSL height and time uncertainties, respectively, and N is the total number of SLIP data at each site.

Since the RSL limiting data constrain height in one direction only, it is difficult to determine the closest point on the model curve to each data point. Therefore, in this case, a simplified approach is taken where the misfit is calculated based on the equation below where the model curve sits on the "wrong" side of the limiting data point (e.g., below a marine limiting point).

$$\delta_{Lim} = \frac{1}{N}\sqrt{\sum_{n=1}^{N}\left(\frac{\Delta}{\sigma}\right)^2_{RSL,n}}\ , \qquad [4]$$

The RSL data in Greenland is not distributed uniformly, and so the data-model misfit can be biased toward regions and time periods with a high density of RSL data (97). Therefore, spatiotemporal weighting is applied such that higher weights are assigned in regions with low data distribution in space and time. To account for spatial variations in data density, we divided the entire region into five subregions (*SI Appendix*, Fig. S8*A*), and the RSL uncertainty is scaled by $\alpha = \sqrt{n/N}$, where n is the number of RSL points in each subregion and N is the total number of Greenland-wide RSL points. To account for variations in temporal data density in a given subregion, the data were divided into four time bins ([0-3 ka], [3-6 ka], [6-9 ka], [9+ ka]), and similar to the spatial weighting, the time uncertainty is scaled by the square root of the number of data in a given bin divided by the total number of data points at that site (97).

Calculating the optimal radial model parameter set is straightforward for the 1D Earth model simulations given the computational efficiency of the calculations. This is not the case for the 3D model, where running many hundreds of model simulations is a major undertaking and highly inefficient. For this reason, we adopted a recently developed emulator (44) to search most of the radial viscosity model parameter space. In this approach, we selected 48 radial viscosity model parameter sets (from a possible 484) to generate Seakon model output with which to train the emulator (*SI Appendix*, Fig. S16). The trained emulator was then used to predict RSL for the remaining 436 model parameter sets. The emulated RSL values were compared to RSL data to find the best-fitting 1D radial viscosity model when considering our lateral viscosity model (see above). Based on the results of this broad parameter search, we identified a much smaller region of the parameter space (comprising 16 parameter sets) that produced optimal fits to the RSL data. The Seakon model was run for these 16 cases and an optimal parameter set determined based on the lowest misfit values: 71 km lithosphere, 10^{21} Pas upper and lower mantle viscosity (*SI Appendix*, Fig. S17).

Data, Materials, and Software Availability. Zip file data have been deposited in Zendoo (DOI: 10.5281/zenodo.16584413) (98). Previously published data were used for this work (http://dx.doi.org/10.1029/2023GL104851) (99).

ACKNOWLEDGMENTS. This work was supported by the Natural Sciences and Engineering Research Council of Canada and the University of Ottawa.

Author affiliations: [a]Department of Earth and Environmental Sciences, University of Ottawa, Ottawa, K1N 6N5, Canada; [b]Faculty of Geo-Information Science and Earth Observation (ITC), Department of Applied Earth Sciences, University of Twente, Enschede 7500 AE, Netherlands; [c]ARC Centre of Excellence for Core to Crust Fluid Systems, Department of Earth and Environmental Sciences, Macquarie University, North Ryde, NSW 2109, Australia; [d]Seakon, Toronto, ON, Canada; [e]Department of Glaciology and Climate, Geological Survey of Denmark and Greenland (GEUS), Copenhagen 1350, Denmark; [f]Planetary magnetospheres laboratory, NASA Goddard Space Flight Center, Greenbelt, MD 20771; [g]Department of Astronomy, University of Maryland College Park, Greenbelt, MD 20742; and [h]Department of Geography, Durham university, Durham DH1 3LE, United Kingdom

1. N. Henriksen, J. Chalmers, C. Friend, *Geological History of Greenland: Four Billion Years of Earth Evolution* (Geological Survey of Denmark and Greenland, 2008).
2. W. Jason Morgan, Hotspot tracks and the early rifting of the Atlantic. *Tectonophysics* **94**, 123–139 (1983).
3. R. D. Muller, J. Y. Royer, L. A. Lawver, Revised plate motions relative to the hotspots from combined Atlantic and Indian Ocean hotspot tracks. *Geology* **21**, 275–278 (1993).
4. I. Rogozhina, Z. Martinec, J. M. Hagedoorn, M. Thomas, K. Fleming, On the long-term memory of the Greenland Ice Sheet. *J. Geophys. Res. Earth Surf.* **116**, e2010JF001787 (2011).
5. J. A. MacGregor *et al*., A synthesis of the basal thermal state of the Greenland Ice Sheet. *J. Geophys. Res. Earth Surf.* **121**, 1328–1350 (2016).
6. R. B. Alley *et al*., Possible role for tectonics in the evolving stability of the Greenland Ice Sheet. *J. Geophys. Res. Earth Surf.* **124**, 97–115 (2019).
7. M. Zeitz, J. M. Haacker, J. F. Donges, T. Albrecht, R. Winkelmann, Dynamic regimes of the Greenland Ice Sheet emerging from interacting melt-elevation and glacial isostatic adjustment feedbacks. *Earth Syst. Dyn.* **13**, 1077–1096 (2022).
8. A. Mordret, Uncovering the Iceland hot spot track beneath Greenland. *J. Geophys. Res. Solid Earth* **123**, 4922–4941 (2018).
9. M. Pourpoint, S. Anandakrishnan, C. J. Ammon, High-resolution Rayleigh wave group velocity variation beneath Greenland. *J. Geophys. Res. Solid Earth* **123**, 1516–1539 (2018).
10. B. Steinberger, E. Bredow, S. Lebedev, A. Schaeffer, Widespread volcanism in the Greenland-north Atlantic region explained by the Iceland plume. *Nat. Geosci.* **12**, 61–68 (2019).
11. N. L. Celli, S. Lebedev, A. J. Schaeffer, C. Gaina, The tilted Iceland plume and its effect on the north Atlantic evolution and magmatism. *Earth Planet. Sci. Lett.* **569**, 117048 (2021).
12. S. K. Antonijevic, J. M. Lees, Effects of the Iceland plume on Greenland's lithosphere: New insights from ambient noise tomography. *Polar Sci.* **17**, 75–82 (2018).
13. I. Rogozhina *et al*., Melting at the base of the Greenland Ice Sheet explained by Iceland hotspot history. *Nat. Geosci.* **9**, 366–369 (2016).
14. Y. M. Martos *et al*., Geothermal heat flux reveals the Iceland hotspot track underneath Greenland. *Geophys. Res. Lett.* **45**, 8214–8222 (2018).
15. R. Steffen, P. Audet, B. Lund, Weakened lithosphere beneath Greenland inferred from effective elastic thickness: A hot spot effect? *Geophys. Res. Lett.* **45**, 4733–4742 (2018).
16. I. M. Artemieva, Lithosphere thermal thickness and geothermal heat flux in Greenland from a new thermal isostasy method. *Earth Sci. Rev.* **188**, 469–481 (2019).
17. B. H. Heyn, C. P. Conrad, On the relation between basal erosion of the lithosphere and surface heat flux for continental plume tracks. *Geophys. Res. Lett.* **49**, e2022GL098003 (2022).
18. J. van den Berg, R. S. W. van de Wal, G. A. Milne, J. Oerlemans, Effect of isostasy on dynamical ice sheet modeling: A case study for Eurasia. *J. Geophys. Res. Solid Earth* **113**, e2007JB004994 (2008).
19. Si. Karato, *Deformation of Earth Materials: An Introduction to the Rheology of Solid Earth* (Cambridge University Press, 2008).
20. L. Tarasov, W. Richard Peltier, Greenland glacial history and local geodynamic consequences. *Geophys. J. Int.* **150**, 198–229 (2002).
21. K. Fleming, K. Lambeck, Constraints on the Greenland ice sheet since the last glacial maximum from sea-level observations and glacial-rebound models. *Quat. Sci. Rev.* **23**, 1053–1077 (2004).
22. B. S. Lecavalier *et al*., A model of Greenland ice sheet deglaciation constrained by observations of relative sea level and ice extent. *Quat. Sci. Rev.* **102**, 54–84 (2014).
23. R. Dietrich *et al*., Jakobshavn isbræ, west Greenland: Flow velocities and tidal interaction of the front area from 2004 field observations. *J. Geophys. Res. Earth Surf.* **112**, e2006JF000601 (2007).
24. S. A. Khan *et al*., Geodetic measurements reveal similarities between post–Last Glacial Maximum and present-day mass loss from the Greenland ice sheet. *Sci. Adv.* **2**, e1600931 (2016).
25. D. Berg *et al*., Vertical land motion due to present-day ice loss from Greenland's and Canada's peripheral glaciers. *Geophys. Res. Lett.* **51**, e2023GL104851 (2024).
26. G. A. Milne *et al*., The influence of lateral Earth structure on glacial isostatic adjustment in Greenland. *Geophys. J. Int.* **214**, 1252–1266 (2018).
27. G. J. G. Paxman, H. C. P. Lau, J. Austermann, B. K. Holtzman, C. Havlin, Inference of the timescale-dependent apparent viscosity structure in the upper mantle beneath Greenland. *AGU Adv.* **4**, e2022AV000751 (2023).
28. M. Weerdesteijn, C. Conrad, Recent ice melt above a mantle plume track is accelerating the uplift of southeast Greenland. *Commun. Earth Environ.* **5**, 791 (2024).
29. S. Adhikari *et al*., Decadal to centennial timescale mantle viscosity inferred from modern crustal uplift rates in Greenland. *Geophys. Res. Lett.* **48**, e2021GL094040 (2021).
30. J. C. Afonso *et al*., 3-D multiobservable probabilistic inversion for the compositional and thermal structure of the lithosphere and upper mantle. I: A priori petrological information and geophysical observables. *J. Geophys. Res. Solid Earth* **118**, 2586–2617 (2013).
31. J. C. Afonso, J. Fullea, Y. Yang, J. Connolly, A. Jones, 3-D multi-observable probabilistic inversion for the compositional and thermal structure of the lithosphere and upper mantle. II: General methodology and resolution analysis. *J. Geophys. Res. Solid Earth* **118**, 1650–1676 (2013).
32. J. C. Afonso *et al*., Thermochemical structure and evolution of cratonic lithosphere in central and southern Africa. *Nat. Geosci.* **15**, 1–6 (2022).
33. J. C. Afonso *et al*., 3-d multiobservable probabilistic inversion for the compositional and thermal structure of the lithosphere and upper mantle: III. Thermochemical tomography in the western-central U.S. *J. Geophys. Res. Solid Earth* **121**, 7337–7370 (2016).
34. P. Ajourlou, F. Darbyshire, P. Audet, G. A. Milne, Structure of the crust and upper mantle in Greenland and northeastern Canada: Insights from anisotropic Rayleigh-wave tomography. *Geophys. J. Int.* **239**, 329–350 (2024).
35. A. Wansing, J. Ebbing, M. Moorkamp, The lithospheric structure of Greenland from a stepwise forward and inverse modelling approach. *Geophys. J. Int.* **238**, 719–741 (2024).
36. L. M. Larsen *et al*., Age of Tertiary volcanic rocks on the West Greenland continental margin: Volcanic evolution and event correlation to other parts of the North Atlantic Igneous Province. *Geol. Mag.* **153**, 487–511 (2016).
37. A. Cox, R. Hart, *Plate Tectonics: How It Works* (Wiley-Blackwell, 1986).
38. L. A. Lawver, R. D. Muller, Iceland hotspot track. *Geology* **22**, 311–314 (1994).
39. B. Steinberger, R. Sutherland, R. O'Connell, Prediction of emperor-Hawaii seamount locations from a revised model of plate motion and mantle flow. *Nature* **430**, 167–73 (2004).
40. C ONeill, D Müller, B Steinberger,, On the uncertainties in hot spot reconstructions and the significance of moving hot spot reference frames. *Geochem. Geophys. Geosyst.* **6**, e2004GC000784 (2005).
41. P. V. Doubrovine, B. Steinberger, T. H. Torsvik, Absolute plate motions in a reference frame defined by moving hot spots in the Pacific, Atlantic, and Indian Oceans. *J. Geophys. Res. Solid Earth* **117**, e2011JB009072 (2012).
42. P. R. Dawes, The bedrock geology under the Inland Ice: The next major challenge for Greenland mapping. *GEUS Bull.* **17**, 57–60 (2009).
43. K. Latychev *et al*., Glacial isostatic adjustment on 3-D earth models: A finite-volume formulation. *Geophys. J. Int.* **161**, 421–444 (2005).
44. R. Love *et al*., A fast surrogate model for 3d-earth glacial isostatic adjustment using tensorflow (v2.8.10) artificial neural networks. *EGUsphere* **2024**, 1–25 (2024).
45. A. Paulson, S. Zhong, J. Wahr, Modelling post-glacial rebound with lateral viscosity variations. *Geophys. J. Int.* **163**, 357–371 (2005).
46. H. C. P. Lau, B. K. Holtzman, "measures of dissipation in viscoelastic media" extended: Toward continuous characterization across very broad geophysical time scales. *Geophys. Res. Lett.* **46**, 9544–9553 (2019).
47. S. A. Woodroffe *et al*., Radiocarbon dating of mangrove sediments to constrain Holocene relative sea-level change on Zanzibar in the southwest Indian Ocean. *Holocene* **25**, 820–831 (2015).
48. R. Steffen *et al*., Early Holocene Greenland-ice mass loss likely triggered Earthquakes and Tsunami. *Earth Planet. Sci. Lett.* **546**, 116443 (2020).
49. G. Sinclair *et al*., Diachronous retreat of the Greenland ice sheet during the last deglaciation. *Quat. Sci. Rev.* **145**, 243–258 (2016).
50. M. J. Simpson, G. A. Milne, P. Huybrechts, A. J. Long, Calibrating a glaciological model of the Greenland Ice Sheet from the last glacial maximum to present-day using field observations of relative sea level and ice extent. *Quat. Sci. Rev.* **28**, 1631–1657 (2009).
51. B. S. Lecavalier *et al*., High arctic Holocene temperature record from the Agassiz ice cap and Greenland Ice Sheet evolution. *Proc. Natl. Acad. Sci. U.S.A.* **114**, 5952–5957 (2017).
52. L. Pan, J. X. Mitrovica, G. A. Milne, M. J. Hoggard, S. A. Woodroffe, Timescales of glacial isostatic adjustment in Greenland: Is transient rheology required? *Geophys. J. Int.* **237**, 989–995 (2024).
53. K. Kjeldsen *et al*., Spatial and temporal distribution of mass loss from the Greenland ice sheet since ad 1900. *Nature* **528**, 396–400 (2015).
54. B. Marzeion, P. W. Leclercq, J. G. Cogley, A. H. Jarosch, Brief communication: Global reconstructions of glacier mass change during the 20th century are consistent. *Cryosphere* **9**, 2399–2404 (2015).
55. K. H. Kjaer *et al*., Glacier response to the little ice age during the neoglacial cooling in Greenland. *Earth Sci. Rev.* **227**, 103984 (2022).
56. A. Glueder *et al*., Calibrated relative sea levels constrain isostatic adjustment and ice history in northwest Greenland. *Quat. Sci. Rev.* **293**, 107700 (2022).
57. A. Aschwanden *et al*., Contribution of the Greenland Ice Sheet to sea level over the next millennium. *Sci. Adv.* **5**, eaav9396 (2019).
58. C. Böning, E. Behrens, A. Biastoch, K. Getzlaff, J. Bamber, Emerging impact of Greenland meltwater on Deepwater formation in the north Atlantic Ocean. *Nat. Geosci.* **9**, pages523–pages527 (2016).
59. IP on Climate Change (IPCC), *Ocean, Cryosphere and Sea Level Change* (Cambridge University Press, 2023), pp. 1211–1362.
60. A. Tarantola, *Inverse Problem Theory and Methods for Model Parameter Estimation* (Society for Industrial and Applied Mathematics, 2005).
61. P. Ajourlou, "Improving models of earth structure in Greenland," Ph.D. thesis, University of Ottawa (2025). https://doi.org/10.20381/ruor-30768.
62. M. Tork Qashqai, J. C. Afonso, Y. Yang, Physical state and structure of the crust beneath the western-central united states from multiobservable probabilistic inversion. *Tectonics* **37**, 3117–3147 (2018).
63. F. Salajegheh *et al*., The lithosphere-asthenosphere system beneath the north Atlantic and surroundings: Results from multi-observable probabilistic inversions. *Geochem. Geophys. Geosyst.* **26**, e2024GC011724 (2025).
64. H. Haario, M. Laine, A. Mira, E. Saksman, Dram: Efficient adaptive MCMC. *Stat. Comput.* **16**, 339–354 (2006).
65. M. Tork Qashqai, J. Carlos Afonso, Y. Yang, The crustal structure of the Arizona transition zone and southern Colorado plateau from multiobservable probabilistic inversion. *Geochem. Geophys. Geosyst.* **17**, 4308–4332 (2016).
66. Z. Guo, J. C. Afonso, M. T. Qashqai, Y. Yang, Y. J. Chen, Thermochemical structure of the north China craton from multi-observable probabilistic inversion: Extent and causes of cratonic lithosphere modification. *Gondwana Res.* **37**, 252–265 (2016).
67. B. Shan *et al*., The thermochemical structure of the lithosphere and upper mantle beneath south China: Results from multiobservable probabilistic inversion. *J. Geophys. Res. Solid Earth* **119**, 8417–8441 (2014).
68. J. C. Afonso, M. Fernàndez, G. Ranalli, W. L. Griffin, J. A. D. Connolly, Integrated geophysical-petrological modeling of the lithosphere and sublithospheric upper mantle: Methodology and applications. *Geochem. Geophys. Geosyst.* **9**, e2007GC001834 (2008).
69. J. C. Afonso, S. Zlotnik, *The Subductability of Continental Lithosphere: The Before and After Story* (Springer, Berlin Heidelberg, Berlin, Heidelberg, 2011), pp. 53–86.
70. M. Ballmer, J. van Hunen, P. Tackley, G. Ito, Spatial and temporal variability in Hawaiian hotspot volcanism induced by small-scale convection. *Nat. Geosci.* **4**, 457–460 (2011).
71. T. Gerya, *Introduction to Numerical Geodynamic Modelling* (Cambridge University Press, 2010).
72. J. van Wijk *et al*., Small-scale convection at the edge of the Colorado Plateau: Implications for topography, magmatism, and evolution of Proterozoic lithosphere. *Geology* **38**, 611–614 (2010).
73. P. D. S. Zlotnik, J. C. Afonso, M. Fernández, Small-scale gravitational instabilities under the oceans: Implications for the evolution of oceanic lithosphere and its expression in geophysical observables. *Philos. Mag.* **88**, 3197–3217 (2008).
74. E. Goldberg, M. Circuns i Duxans, O. Ortega Gelabert, M. J. Mantsinen, A. Soba, Validating neutro, a deterministic finite element neutron transport solver for fusion applications, with literature tests, experimental benchmarks and other neutronic codes. *Plasma Phys. Control. Fusion* **64**, 104006 (2022).

75. F. Lavoue, S. Lebedev, N. Celli, A. Schaeffer, *Radially and Azimuthally Anisotropic Shear-Wave Velocity Model Of The Earth's Upper Mantle* (EGU General Assembly Conference Abstracts, 2021), pp. EGU21-14987.
76. N. A. Simmons, A. M. Forte, L. Boschi, S. P. Grand, Gypsum: A joint tomographic model of mantle density and seismic wave speeds. *J. Geophys. Res. Solid Earth* **115**, e2010JB007631 (2010).
77. R. Pail *et al.*, Short note: The experimental geopotential model xgm2016. *J. Geod.* **92**, 443–451 (2018).
78. F. Lucazeau, Analysis and mapping of an updated terrestrial heat flow data set. *Geochem. Geophys. Geosyst.* **20**, 4001–4024 (2019).
79. G. Laske, G. Masters, Z. Ma, M. Pasyanos, Update on CRUST1.0 - A 1-degree global model of Earth's crust. *Geophys. Res. Abstr.* **15**, 2658 (2013).
80. M. Morlighem *et al.*, IceBridge BedMachine Greenland (Version 5, Boulder, Colorado, 2022), https://doi.org/10.5067/GMEVBWFLWA7X. Accessed 13 November 2025.
81. D. Farinotti *et al.*, A consensus estimate for the ice thickness distribution of all glaciers on Earth. *Nat. Geosci.* **12**, 168–173 (2019).
82. M. C. Manassero *et al.*, Lithospheric structure and melting processes in southeast Australia: New constraints from joint probabilistic inversions of 3D magnetotelluric and seismic data. *J. Geophys. Res. Solid Earth* **129**, e2023JB028257 (2024).
83. J. Ritsema, A. Deuss, H. J. van Heijst, J. H. Woodhouse, S40RTS: A degree-40 shear-velocity model for the mantle from new Rayleigh wave dispersion, teleseismic traveltime and normal-mode splitting function measurements. *Geophys. J. Int.* **184**, 1223–1236 (2011).
84. A. J. Schaeffer, S. Lebedev, Global shear speed structure of the upper mantle and transition zone. *Geophys. J. Int.* **194**, 417–449 (2013).
85. J. Austermann, J. Mitrovica, K. Latychev, G. Milne, Barbados-based estimate of ice volume at last glacial maximum affected by subducted plate. *Nat. Geosci.* **6**, 553–557 (2013).
86. J. C. Afonso, F. Salajegheh, W. Szwillus, J. Ebbing, C. Gaina, A global reference model of the lithosphere and upper mantle from joint inversion and analysis of multiple data sets. *Geophys. J. Int.* **217**, 1602–1628 (2019).
87. W. R. Peltier, The impulse response of a maxwell earth. *Rev. Geophys.* **12**, 649–669 (1974).
88. J. X. Mitrovica, W. R. Peltier, A comparison of methods for the inversion of viscoelastic relaxation spectra. *Geophys. J. Int.* **108**, 410–414 (1992).
89. J. Mitrovica, G. Milne, On post-glacial sea level: I. General theory. *Geophys. J. Int.* **154**, 253–267 (2003).
90. R. Kendall, J. Mitrovica, G. Milne, On post-glacial sea level - II. Numerical formulation and comparative results on spherically symmetric models. *Geophys. J. Int.* **161**, 679–706 (2005).
91. G. A. Milne, J. X. Mitrovica, Postglacial sea-level change on a rotating earth. *Geophys. J. Int.* **133**, 1–19 (1998).
92. J. X. Mitrovica, J. Wahr, I. Matsuyama, A. Paulson, The rotational stability of an ice-age earth. *Geophys. J. Int.* **161**, 491–506 (2005).
93. E. Ivins, T. James, Antarctic glacial isostatic adjustment: A new assessment. *Antarct. Sci.* **17**, 541–553 (2005).
94. J. E. Box, Survey of Greenland instrumental temperature records: 1873–2001. *Int. J. Climatol.* **22**, 1829–1847 (2002).
95. A. Bartholet, G. Milne, K. Latychev, Modelling sea-level fingerprints of glaciated regions with low mantle viscosity. *Earth Syst. Dyn.* **12**, 783–795 (2021).
96. J. X. Mitrovica, A. M. Forte, M. Simons, A reappraisal of postglacial decay times from Richmond Gulf and James Bay. *Canada. Geophys. J. Int.* **142**, 783–800 (2000).
97. R. D. Briggs, L. Tarasov, How to evaluate model-derived deglaciation chronologies: A case study using antarctica. *Quat. Sci. Rev.* **63**, 109–127 (2013).
98. P. Ajourlou *et al.*, Greenland Earth structure and GIA models datasets. *Zenodo*. https://zenodo.org/records/16584413. Deposited 30 July 2025.
99. D. Berg *et al.*, Vertical Land Motion Due To Present-Day Ice Loss From Greenland's and Canada's Peripheral Glaciers. AGU (2024). http://dx.doi.org/10.1029/2023GL104851. Accessed 3 December 2023.